

Revisiting MAE pre-training for 3D medical image segmentation

Tassilo Wald^{*1,2,3}, Constantin Ulrich^{*1,4,5}, Stanislav Lukyanenko⁶, Andrei Goncharov⁶,
Alberto Paderno^{6,7}, Leander Maerkisch⁶, Paul Jaeger^{8,9}, Klaus Maier-Hein^{1,2,3,4,5,8}

¹ Division of Medical Image Computing, German Cancer Research Center (DKFZ); ² Helmholtz Imaging, DKFZ

³ Faculty of Mathematics and Computer Science, University of Heidelberg; ⁴ Medical Faculty Heidelberg, University of Heidelberg

⁵ National Center for Tumor Diseases (NCT), NCT Heidelberg; ⁶ FLOY, Munich, Germany

⁷ Department of Biomedical Sciences, Humanitas University (Milan), IRCCS Humanitas Research Hospital, Rozzano, Italy.

⁸ Interactive Machine Learning Group, DKFZ Heidelberg; ⁹ Pattern Analysis and Learning Group, Department of Radiation Oncology

tassilo.wald@dkfz-heidelberg.de

Abstract

Self-Supervised Learning (SSL) presents an exciting opportunity to unlock the potential of vast, untapped clinical datasets, for various downstream applications that suffer from the scarcity of labeled data. While SSL has revolutionized fields like natural language processing and computer vision, its adoption in 3D medical image computing has been limited by three key pitfalls: Small pre-training dataset sizes, architectures inadequate for 3D medical image analysis, and insufficient evaluation practices. In this paper, we address these issues by i) leveraging a large-scale dataset of 39k 3D brain MRI volumes and ii) using a Residual Encoder U-Net architecture within the state-of-the-art nnU-Net framework. iii) A robust development framework, incorporating 5 development and 8 testing brain MRI segmentation datasets, allowed performance-driven design decisions to optimize the simple concept of Masked Auto Encoders (MAEs) for 3D CNNs. The resulting model not only surpasses previous SSL methods but also outperforms the strong nnU-Net baseline by an average of approximately 3 Dice points setting a new state-of-the-art. Our code and models are made available [here](#).

1. Introduction

In recent years, the concept of Self-Supervised Learning (SSL) has emerged as a driving factor in data-rich domains, enabling large-scale pre-training that facilitates the learning of robust and transferable general-purpose representations [2, 14, 25]. This paradigm shift has been instrumental in advancing various fields, particularly in domains with abundant labeled data like NLP or natural vision. In the

^{*}Equal contribution. Authors are permitted to list their name first in their CVs.

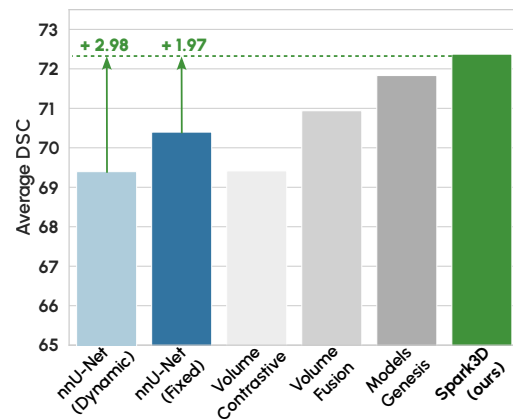


Figure 1. **Well-configured MAE pre-training for CNNs is state-of-the-art.** When comparing our MAE pre-trained model on all eleven test Datasets, Spark3D achieves almost +3 DSC points compared to the strong nnU-Net baseline and outperforms current SSL methods.

domain of 3D medical image computing, this trend has not caught on. Currently, the domain is either focused on training from-scratch, mainly using the nnU-Net framework by Isensee et al. [18], or using supervised pre-training, which is limited by the cost associated with annotated data [17, 35, 40]. The usage of supervised pre-training implies the willingness of the domain to adopt pre-training and calls to question the currently established SSL methods in the domain. We believe this lack of widespread adoption of previously established methods can be attributed to three major pitfalls of previous SSL research in this field:

P1 - Limited dataset size: Many SSL approaches have been developed on very few unlabeled volumes, often being trained on fewer than 10,000 images [12, 30, 31, 42, 44, 45], almost approaching scales of supervised dataset sizes.

These datasets tend to be pooled from publicly available annotated datasets, as larger datasets pose a greater hurdle to acquire. While many hospitals possess 3D medical images in the millions, they are locked away from the public due to patient privacy concerns. Some larger open-source datasets exist, e.g., the Adolescent Brain Cognitive Decline (ABCD) dataset of the NIH (N=40k) or the UK Biobank (UK-BB) (N=120k), but they restrict access pending an internal review board’s approval, posing a hurdle for open science.

P2 - Outdated Backbones: Many studies develop their SSL method on non-state-of-the-art architectures, e.g., utilizing transformers [5, 31, 39, 42]. While transformers are prevalent in the 2D natural imaging domain [8], recent architectures leveraging attention [36] have so far not been able to reach state-of-the-art performance in 3D medical segmentation. In fact, well-configured 3D U-Net [6, 27] inspired CNNs dominate 3D medical image segmentation, outperforming transformer-based models by a large margin [19]. This underscores the need for SSL methods that can be seamlessly integrated with CNNs to harness their full potential in medical image analysis on downstream tasks.

P3 - Insufficient Evaluation: Existing methods often lack rigorous evaluation, masking the methods’ efficacy. This is represented through: i) Evaluating on too few datasets to show generalization of the pre-training ii) Stacking multiple contributions, e.g., novel architecture with new pre-training, which does not allow one to draw conclusions if the pre-training is effective without the architecture [39] iii) Comparing to bad from-scratch baselines, like a badly configured, outdated [6] model instead of a well-configured 3D nnU-Net CNN baseline [18]. iv) Evaluating their method on seen data they pre-trained on. We want to emphasize that we do not intend to point fingers, but to raise awareness that evaluation matters and insufficient evaluation can lead to a lack of clarity which methods are the best. This observation is similar to the recent study by Isensee et al. [19], that shows that this is also prevalent in the field of medical image segmentation when training from-scratch.

In this paper, we explore the Masked Auto Encoder (MAE) paradigm for 3D CNNs, with the recent adaptations introduced by Tian et al. [32], Woo et al. [41]. Our approach addresses the key pitfalls of previous SSL research in 3D medical image segmentation, ensuring broader applicability and higher performance. Our main contributions are as follows:

- State-of-the-Art Performance:** Our final model achieves superior performance compared to existing SSL-pre-trained models using the same architecture and dataset, see Fig. 1. Notably, this is the first work to demonstrate that SSL pretraining with a fixed architecture can consistently outperform a state-of-the-art, dynamically optimized nnU-Net baseline by approximately 3 Dice points across 11 diverse downstream datasets

Table 1. **Current SSL methods are limited by three pitfalls:** They are trained on less than 10K 3D images (P1), they do not use a state-of-the-art backbone for 3D image segmentation as recommended by Isensee et al. [19] (P2) or they do not evaluate their method on more than 4 downstream datasets (P3). indicates evading a pitfall while indicates falling for a pitfall.

| Method | Year | P1 | P2 | P3 |
|-----------------|------------|-------------------------------------|-------------------------------------|-------------------------------------|
| | | Data | Model | Eval. |
| 3DMAE [5] | Jan. 2023 | <input type="checkbox"/> | <input type="checkbox"/> | <input type="checkbox"/> |
| GL-MAE [45] | Aug. 2023 | <input type="checkbox"/> | <input type="checkbox"/> | <input checked="" type="checkbox"/> |
| MAPSeg [43] | March 2023 | <input type="checkbox"/> | <input type="checkbox"/> | <input type="checkbox"/> |
| HySparK [30] | Aug. 2024 | <input type="checkbox"/> | <input checked="" type="checkbox"/> | <input checked="" type="checkbox"/> |
| AMAES [23] | Aug. 2024 | <input checked="" type="checkbox"/> | <input checked="" type="checkbox"/> | <input type="checkbox"/> |
| Swin UNETR [31] | March 2022 | <input type="checkbox"/> | <input type="checkbox"/> | <input checked="" type="checkbox"/> |
| VoCo [42] | April 2024 | <input type="checkbox"/> | <input type="checkbox"/> | <input checked="" type="checkbox"/> |
| VF [39] | June 2023 | <input checked="" type="checkbox"/> | <input type="checkbox"/> | <input type="checkbox"/> |
| MG [44] | Aug. 2019 | <input type="checkbox"/> | <input type="checkbox"/> | <input checked="" type="checkbox"/> |
| GVSL [15] | March 2023 | <input type="checkbox"/> | <input type="checkbox"/> | <input checked="" type="checkbox"/> |
| S3D (ours) | | <input checked="" type="checkbox"/> | <input checked="" type="checkbox"/> | <input checked="" type="checkbox"/> |

- [18]. An associated model will be made available.
- Comprehensive Evaluation Addressing Previous Pitfalls:** Building on the detailed analysis of limitations in prior work (see Tab. 1), we set up a robust development environment to design our method. (i) P1: We utilize a collection of 39k 3D MRI volumes for self-supervised pre-training, substantially larger than most datasets used in prior SSL work [12, 30, 31, 42, 44, 45]. (ii) P2: By using the state-of-the-art Residual Encoder U-Net CNN architecture [19], we bypass the limitations of outdated or transformer-based architectures, leveraging CNNs’ superior performance in 3D medical segmentation. (iii) P3: We rigorously evaluate our model across five development and eight testing datasets, covering a wide range of downstream tasks, diverse pathologies, novel image modalities, and multi-center datasets. Moreover, we disentangle pre-training methodology from other contributions like novel backbones and include the strong 3D nnU-Net baseline, ensuring reliable results.
- In-Depth Ablation Studies:** We provide detailed analyses of critical design decisions, such as masking ratio, sparsification, and fine-tuning strategies. Additional ablations explore generalization, low-data performance, and faster fine-tuning, offering valuable insights.

While the fundamental concept of an MAE is not novel, its application in 3D medical image analysis has yet to be fully validated due to limitations in previous studies, which we illustrate in Tab. 1. Our carefully designed experiments close these gaps and reveal MAEs true potential.

2. Development Framework

The goal of this paper is to develop a robust SSL pre-training method. Due to the limited prior work in the 3D medical domain, many design choices need to be made. We address this by sequentially validating each methodological contribution on five downstream development datasets before testing the final configuration on eight untouched test datasets. To reduce the search space and disentangle the effects of SSL pre-training from other basic design choices, we choose to keep some parameters fixed based on best practices in the domain:

(i) The architecture used is always the same state-of-the-art residual encoder U-Net architecture (ResEnc U-Net) [19, 35]. (ii) The input patch size is set to [160x160x160]. (iii) All images are resampled to the same target spacing of [1x1x1] mm [28]. (iv) All images are z-score normalized to zero mean and unit variance [18]. (v) As optimizer, we use SGD with a decreasing poly-learning rate [4] following nnU-Net [18]. (vi) We always employ random sampling during pre-training, irrespective of the prevalence of the different MR modalities.

Pre-training Dataset To develop our pre-training method, we utilize a proprietary brain MRI dataset sourced from over 44 centers containing over 9k patients comprising a total of approx. 44k 3D MRI scans. Due to the variety of data sources, this dataset contains images from more than 10 different MR scanners, various MR modalities and a diverse patient population. For more details on the distributions, we refer to Figure 3.

Since this data is sourced directly from clinical examinations, it includes empty or broken images, poor-quality images and so-called scout scans used to determine the field of view of the patient in the MR. Since these scans are not used in diagnostics, these images are filtered by discarding (a) images with a field of view of $< 50mm$ in any axis, (b) images with a spacing $> 6.5mm$ in any direction and (c) images of file size $< 200kb$, which indicate an empty image. Moreover due to the low quantity of MR Angiography, Susceptibility weighted Images (SWI) and Proton Density (PD) weighted images, we restrict our training data to only include T1, T2, T1 FLAIR and T2 FLAIR images, resulting in our final pre-training dataset of 39,168 MR images.

Development Datasets After pre-training we fine-tune on five datasets and calculate the average Dice Similarity Coefficient (DSC) per dataset to evaluate the effectiveness of the pre-training. The multiple datasets are essential to ensure that our design choices do not overfit to a specific MRI modality or pathological target. Specifically, we utilize:

1. *MS FLAIR (D1)*: Consensus delineations of multiple sclerosis (MS) lesions on T2-weighted FLAIR images [24].
 2. *Brain Mets (D2)*: Brain metastases imaged through T1, contrast enhanced gradient echo T1ce, contrast enhanced spin echo T1 and a T2 FLAIR sequence acquired in the Stanford University Hospital [11].
 3. *Hippocampus (D3)*: The Hippocampus dataset, task 4 of the medical segmentation decathlon (MSD) [1], contains delineations of the anterior and posterior Hippocampus in T1 weighted MRI [29].
 4. *Atlas22 (D4)*: Anatomical Tracings of Lesions After Stroke (ATLAS) on T1 weighted images. We use the Atlas R2.0 dataset from Liew et al. [22].
 5. *CrossModa (D5)*: Delineations of intra-meatal and extra-meatal vestibular schwannoma tumors and cochlea delineations in contrast-enhanced T1 weighted MRI [7].
- Of all these datasets, we set aside a hold-out test set comprising 20% of all images before the start of the method development process. The remaining images were split 80/20 into training and validation sets for the development process.

Test Datasets Additionally, eight hold-out test sets were used to evaluate the efficacy of our learned representations when fine-tuning them to segment other target structures.

1. *Cosmos (D6)*: This dataset features carotid vessel wall segmentation and atherosclerosis diagnosis, of which we use the contours to evaluate segmentation performance [3].
2. *HaNSeg (D7)*: This dataset contains segmentations of 30 organs at risk (OAR), with associated T1 MRI and CT, of which we only use the MR images for model development [26].
3. *Isles22 (D8)*: This dataset contains annotations of ischemic stroke lesions, with associated diffusion-weighted imaging (DWI), apparent diffusion coefficient (ADC) and T2 FLAIR [16].
4. *HNTS-MRG24 (D9)*: T2-weighted MR images of pre-treatment oropharyngeal cancer and metastatic lymph nodes with associated annotations [38].
5. *BraTS Africa (D10)*: This dataset contains 1.5 Tesla T1, T1ce, T2, and T2 FLAIR MRIs of glioblastoma and high-grade gliomas imaged in Nigeria.
6. *T2 Aneurysms (D11)*: This proprietary dataset contains 240 T2 MRI images of segmented brain aneurysms with the surrounding brain tissue.
7. *TOF Angiography Aneurysms (D12)*: This proprietary dataset contains 144 time-of-flight MR-angiography images of segmented brain aneurysms with the surrounding brain tissue.
8. *BraTS Mets (D13)*: This dataset holds brain metastases segmentations on T1ce MRIs, similar to D2. However,

instead of fine-tuning on it we use it to measure generalization when inferring models trained on *D2* on it.

For test datasets *D6-D12* we use an 80/20 split for fine-tuning and for testing. A validation set is omitted as we fine-tune each method only once without any interventions. For *D13* all data is used for testing, as no training is conducted.

3. Related Work

In this section, we revisit currently established MAE pre-training paradigms. Then, we survey existing MAE pre-training paradigms in the 3D medical domain, before expanding this to a broader set of pre-training paradigms for 3D medical image segmentation.

3.1. Masked Autoencoders

Auto-encoders have been established for a long time through the early pioneering works of Vincent et al. [37] but recently garnered significant attention through He et al. [14], showing that a simple MAE pre-training paradigm is scalable and provides substantial performance improvements. Subsequently, follow-up works extended these findings to video data [9, 34] as well as language-image data [21]. These earlier successes primarily relied on Transformer architectures, as their sequence modeling offered significant VRAM savings. CNNs on the other hand are less suited to such a pre-training paradigm as masking disrupts the 2D data-structure they compute on. Despite this Woo et al. [41] and Tian et al. [32] were able to extend MAE pre-training successfully to CNNs. Woo et al. [41] introduced their fully convolutional masked autoencoder (FC-MAE) framework, while Tian et al. [32] introduced adaptations to the convolution computation and normalization to make it resilient to masking.

3.2. Masked Autoencoder In 3D Medical

The earliest work using autoencoders for self-supervised pre-training in the medical domain was Models Genesis (MG) conducted by Zhou et al. [44] in 2019. They introduced reconstruction of in-painting, out-painting, and denoising of local intensity shifts as their pre-training task. Many approaches followed, with Swin UNETR by Tang et al. [31] proposing a joint in-painting, rotation, and contrastive objective for Swin Transformer pre-training. Chen et al. [5] proposed a basic masking and reconstruction strategy applied to 3D Vision Transformers (ViT) [8] termed (3DMAE) and Zhuang et al. [45] proposed to use a combination of masked global and local views in conjunction with a reconstruction and consistency loss to pre-train 3D ViTs, named GL-MAE. MAPSeg by Zhang et al. [43] combines a masked autoencoder objective and pseudo-labeling to address domain shifts in a federated setting. More recently, in concurrent work, Munk et al. [23] proposed pre-training

CNNs with a vanilla masking and reconstruction objective without any adaptations on a large brain dataset (AMAES) and Tang et al. [30] presented a sparse MAE with reconstruction objective pre-trained on abdomen CT data (HyS-parK).

3.3. Other Pre-Training For 3D Medical

Additionally, self-supervised learning approaches for 3D medical images include Zhuang et al. [46], who introduced a training objective aimed at recovering the orientation and rotation of shuffled and rotated sub-volumes, inspired by a Rubik’s cube. Wang et al. [39] proposed a method that involves mixing two images at varying patch rates and predicting the mixing categories via a segmentation objective, termed Volume Fusion (VF). Geometric Visual Similarity Learning (GVSL) of He et al. [15] leveraged anatomical consistency by learning to register two images of the same field of view and using local similarity as a training objective. More recently, Wu et al. [42] suggested partitioning a volume into non-overlapping base-crops and generating additional overlapping sub-crops, with a training objective to predict the degree of overlap between sub-crops and base-crops (VoCo).

4. Revisiting 3D MAEs

Masked autoencoders (MAEs) are a well-established pre-training paradigm in the natural imaging domain and in the medical image segmentation domain for transformers. In this section, we investigate this paradigm and optimize it for 3D medical image segmentation using a ResEnc U-Net architecture of Isensee et al. [19].

Default parameters MAEs are trained by masking an input image to a certain degree and training the network to reconstruct the occluded regions, minimizing deviations between reconstruction and the original image. In our experiments, we train the MAE with an L2-Loss in the z-score normalized voxel space and only calculate the reconstruction loss where regions were masked. Moreover, we do not remove skip-connections, following the general consensus of Woo et al. [41], Tian et al. [32], and He et al. [14]. The default hyperparameters (as used by the model denoted in gray in Tab. 2) are learning rate 1e-2, weight decay 3e-5, batch size 6, SGD optimizer with Nesterov momentum 0.99, masking ratio of 75% trained with a PolyLR schedule for 250k steps (this represent 1000 epochs in the nnU-Net framework) and minor spatial augmentations of affine scaling, rotation and mirroring.

Sparsification When masking the input image, CNNs are not able to ignore the masked regions in the same manner as transformers can. To address this, Tian et al. [32] proposed

Table 2. **Development Experiments:** During development, we evaluate the Average DSC on all development datasets to quantify the best configuration. Methods of the same configuration are denoted through common colors.

(a) **Sparsification:** The introduction of all sparsification components showed best results, with most improvements from adding the additional densification conv layer between encoder and decoder.

| Configuration | D1 | D2 | D3 | D4 | D5 | Avg. D1-D5 |
|----------------------|--------------|--------------|--------------|--------------|--------------|--------------|
| Base | 49.96 | 72.62 | 89.03 | 63.45 | <u>81.67</u> | 71.35 |
| + Sparse Conv. + BN. | <u>50.34</u> | <u>73.34</u> | 88.91 | <u>62.96</u> | 81.25 | 71.36 |
| + w/ Mask Token | 50.02 | 73.21 | <u>88.92</u> | 62.84 | 81.83 | <u>71.37</u> |
| + w/ Dens. Conv. | 51.02 | 74.07 | 88.91 | 62.81 | 81.50 | 71.66 |

(b) **Masking ratio:** Masking ratios between 60% and 75% worked best when choosing static ratios. Overall, a dynamic range, including higher masking ratios, performs the best.

| Mask ratio | D1 | D2 | D3 | D4 | D5 | Avg. D1-D5 |
|------------|--------------|--------------|--------------|--------------|--------------|--------------|
| 30 % | 50.25 | 71.37 | 88.90 | 63.18 | <u>81.70</u> | 71.08 |
| 45 % | 50.60 | 70.83 | <u>88.97</u> | <u>63.27</u> | 81.73 | 71.08 |
| 60 % | 50.62 | 73.56 | 88.96 | 63.37 | 81.48 | 71.60 |
| 75 % | <u>51.02</u> | 74.07 | 88.91 | 62.81 | 81.50 | 71.66 |
| 90 % | 50.56 | 72.51 | 88.98 | 62.41 | 81.49 | 71.19 |
| U[60%-90%] | 51.49 | <u>74.01</u> | 88.83 | 62.39 | 81.54 | <u>71.65</u> |

(c) **Development performance:** When comparing our final S3D model against the baseline methods, trained equally, S3D exceeds all baselines on the development datasets.

| SSL Method | No (Dyn.) | No (Fix.) | S3D* | S3D |
|----------------------|--|--------------|--------------|--------------|
| Dataset | Dice Similarity Coefficient (DSC) | | | |
| MS FLAIR (D1) | 57.81 | <u>59.82</u> | 59.75 | 60.35 |
| Brain Mets (D2) | 63.66 | 56.53 | <u>64.20</u> | 65.24 |
| Hippocampus (D3) | 89.18 | 89.24 | <u>89.45</u> | 89.60 |
| Atlas22 (D4) | 63.28 | 65.52 | <u>66.61</u> | 66.95 |
| CrossModa (D5) | 85.64 | 83.44 | 83.61 | <u>84.08</u> |
| Cosmos22 (D6) | 60.28 | 78.17 | 80.01 | <u>80.00</u> |
| ISLES22 (D7) | 77.94 | <u>79.44</u> | 78.94 | 79.70 |
| Hanseg (D8) | 59.00 | <u>61.85</u> | 61.27 | 62.11 |
| HNTS-MRG24 (D9) | 66.73 | 65.90 | <u>67.03</u> | 68.62 |
| BRATS24 Africa (D10) | 93.07 | <u>92.51</u> | 92.49 | 92.19 |
| Avg. DSC | 71.66 | 73.24 | <u>74.34</u> | 74.88 |
| Avg. Rank | 3.2 | 2.9 | <u>2.4</u> | 1.5 |

to adapt the CNN architectures to better fit the sparse inputs:

(a) **Sparse Convolutions and Normalization:** Through the receptive field of convolutions masked-out regions are iteratively eroded from their boundaries. By re-applying the masked regions after every convolution this problem can be resolved. Moreover, the masks can introduce a problematic shift in the normalization layer statistics due to the introduced zero values. To resolve this normalization is constrained to only consider the non-masked values. (b) **Mask Token:** Instead of feeding the light-weight decoder feature maps with zeroed mask regions, the regions are densified by filling them with a learnable mask token, simplifying the reconstruction task of the decoder. (c) **Densification Convolution:** After filling the masks with the Mask Token and before passing the feature maps to the decoder, a $[3 \times 3 \times 3]$

convolution is applied to the feature maps at every resolution except the highest resolution to prepare the representations for decoding.

Results of these changes are visualized in Tab. 2a. The adaptations are introduced iteratively, meaning the 'Mask-Token' ablation is only applied together with the Sparse Convolutions and Normalization. It can be observed that the full set of adaptations improves performance by an average of 0.3 DSC points across our development datasets. Subsequently, all adaptations are kept and the following evaluations are presented with these changes applied.

Masking strategy The masked region is determined by sampling randomly in the CNN's bottleneck of shape $[5 \times 5 \times 5]$ and up-sampling these regions to the input resolution, to ensure the masks align in the bottleneck of the CNN architectures. This results in masking regions of $[32 \times 32 \times 32]$ voxels of non-overlapping regions in the input. As a sampling strategy, we follow random masking, as previous work showed no benefit of structured masking for images nor videos [9, 14]. In the scope of the development phase we explore 5 static masking ratios between 30 and 90%, and evaluate a dynamic masking ratio randomly masking between 60% and 90%.

Results are presented in Table Tab. 2b and highlight that the masking ratios of 60%, 75%, and the dynamic masking ratio of 60% to 90% perform equally well. Due to the highly similar performance, we choose to proceed with a dynamic masking ratio over the static masking ratio, due to expecting this masking to be more difficult to learn and with the upcoming scaling experiment in mind. We refer to this model as Spark3D (S3D) going forward.

Fine-tuning strategy Given a pre-trained model, a crucial question arises: Which weights to transfer and how to schedule the fine-tuning? We investigated various different schedules, with all of them implemented in the nnU-Net framework [18]. Regarding weight transfer we investigated transferring (i) both the encoder and decoder \blacktriangleright , or (ii) only the encoder \blacktriangleright with a randomly initialized decoder. Regarding the fine-tuning schedule, we investigate whether to use a learning rate warm-up of 12.5k steps, ramping the learning rate up to the maximum LR. When only transferring the encoder, an additional warm-up of only the decoder is investigated to adapt the randomly initialized decoder to the pre-trained encoder. In some configurations, this results in two learning rate warm-ups of 12.5k steps each. Additionally, we investigate whether to keep the encoder frozen \blacktriangleright for the entire fine-tuning process, or to fine-tuning encoder weights as well. Lastly, we investigate whether to decrease the peak learning rate to $1e - 3$, $1e - 4$ or to keep it at the default of $1e - 2$.

Table 3. **Fine-tuning matters.** We compare various combinations of weight transfer and fine-tuning schedules. Transfer: Transfer all weights, Transfer encoder weights only. Warm-Up and Fine-tuning: Only decoder weights adapted during fine-tuning, Encoder and decoder weights adapted during fine-tuning. ‡: nnU-Net default (Dynamic planning.)

| Transfer | 1. Warm-Up | 2. Warm-Up | Fine-tuning | Max. LR | D1 | D2 | D3 | D4 | D5 | Avg |
|----------|------------|------------|-------------|---------|-------|-------|-------|-------|-------|--------------|
| | - | - | | 1e-2 | 45.56 | 72.26 | 88.80 | 60.44 | 82.61 | 69.93‡ |
| | - | - | | 1e-2 | 49.37 | 69.13 | 88.78 | 60.74 | 81.33 | 69.87 |
| | - | - | | 1e-2 | 50.37 | 70.64 | 88.61 | 61.51 | 81.91 | 70.61 |
| | - | - | | 1e-3 | 49.98 | 71.04 | 88.68 | 61.45 | 82.12 | 70.65 |
| | - | | | 1e-2 | 49.84 | 72.56 | 88.45 | 62.16 | 81.75 | 70.95 |
| | - | | | 1e-3 | 51.54 | 72.74 | 88.85 | 62.44 | 82.33 | <u>71.58</u> |
| | - | | | 1e-4 | 50.66 | 72.98 | 88.68 | 62.73 | 82.09 | 71.43 |
| | - | - | | 1e-2 | 50.81 | 68.55 | 88.52 | 60.73 | 80.77 | 69.87 |
| | - | - | | 1e-3 | 50.11 | 73.90 | 88.58 | 61.82 | 81.48 | 71.18 |
| | - | | | 1e-2 | 51.39 | 72.06 | 88.65 | 61.70 | 81.78 | 71.12 |
| | - | | | 1e-3 | 51.04 | 72.72 | 88.91 | 62.84 | 81.19 | 71.34 |
| | | | | 1e-2 | 48.81 | 72.92 | 88.84 | 62.46 | 82.04 | 71.02 |
| | | | | 1e-3 | 51.42 | 72.84 | 89.09 | 63.30 | 82.15 | 71.76 |
| | | | | 1e-4 | 50.13 | 72.26 | 88.72 | 61.70 | 81.93 | 70.95 |

Results are presented in Table 3 and allow three important observations to be made: (i) **Warm-up stages are essential:** Not applying a warm-up step significantly reduces performance. Including a warm-up for both the encoder and decoder boosts accuracy by 0.6 to 1 DSC points. (ii) **Learning rate adjustments matter:** Reducing the peak learning rate to 1e-3 during fine-tuning consistently yields better results than the default 1e-2, with the best performance seen when fine-tuning both the encoder and decoder with lower learning rates. (iii) **Freezing encoder weights is detrimental:** The encoder should not remain fixed during fine-tuning. Allowing the encoder to be fine-tuned improves the model’s performance compared to when only the decoder is fine-tuned.

5. Results and Discussion

We compare our final model S3D against Volume Contrastive (VoCo) [42], VolumeFusion (VF) by Wang et al. [39], as well as Models Genesis (MG) [44]. The baselines are pre-trained for 250k steps using the same framework on the same data with the same backbone and the same hyperparameters (where possible) but scaled to fully utilize an A100 40GB GPU. We provide explicit baseline methods and configuration details in Appendix A. Moreover, we compare against two strong from-scratch baselines. The first, *No (Dyn.)*, represents a non-pretrained (i.e., from scratch) default nnU-Net 3D *fullres* architecture that was planned and preprocessed on each downstream dataset individually, potentially resulting in different architectures, data preprocessing, and spacings. The second from-scratch baseline, *No (Fixed)*, is a nnU-Net training with the same plans and pre-processing as defined by our

pre-training. The dataset-wise mean DSC and mean NSD values across our test dataset suite are provided in Tab. 4. Additionally, the ranking stability of the methods is evaluated through bootstrapping and is provided in Fig. 2.

5.1. Observations

SSL pre-training works Across all tested datasets, SSL pre-trained methods demonstrate improved downstream segmentation performance. Comparing our S3D method to the most similar from-scratch baseline *No (Fixed)*, we observe higher DSC scores in 10 out of 11 test datasets, with an average increase of +2 DSC points and +1.6 NSD points. This improvement is not limited to our method; MG and VF also achieve higher performance than the baseline, indicating the utility of SSL methods when applied to sufficient data and state-of-the-art architecture.

MAEs dominate Throughout our test dataset pool, SSL schemes using the masked image modeling paradigm (MG and S3D) consistently rank higher than the contrastive VoCo or the pseudo-segmentation-based VolumeFusion pre-training method for CNN pre-training. Given the age of Models Genesis - published in 2019 - it is surprising to see it outperform the more recent VoCo or VF. We attribute this to a combination of two factors: 1. Models Genesis was originally published and trained on an outdated 3D-UNet [6] and outside of the powerful nnU-Net framework [18]. This highlights the importance of avoiding Pitfall 2: Training on a state-of-the-art backbone. 2. VoCo and VF were introduced in conjunction with architectures they were optimized for. By transferring them to a CNN setting, hyperparameters chosen to optimize the method for their original ar-

Table 4. **S3D out-performs all baselines:** The upper table presents the DSC results, while the lower table displays the NSD results across the test datasets, covering a diverse range of brain MRI tasks. *No Fixed* represents a from-scratch baseline sharing the same architecture, preprocessing and downstream training steps as all SSL methods. *No Dyn.* represents the original nnU-Net adapted to each downstream dataset individually.

| SSL Method | No (Dyn.) | No (Fix.) | VoCo | VF | MG | S3D |
|----------------------|--|--------------|--------------|--------------|--------------|--------------|
| Dataset | Dice Similarity Coefficient (DSC) | | | | | |
| MS FLAIR (D1) | 57.81 | 59.82 | 59.70 | 59.29 | 58.64 | 60.35 |
| Brain Mets (D2) | 63.66 | 56.53 | 56.25 | 61.01 | 65.39 | 65.24 |
| Hippocampus (D3) | 89.18 | 89.24 | 88.78 | 89.03 | 89.38 | 89.60 |
| Atlas22 (D4) | 63.28 | 65.52 | 62.97 | 65.76 | 65.93 | 66.95 |
| CrossModa (D5) | 85.64 | 83.44 | 83.07 | 84.24 | 83.91 | 84.08 |
| Cosmos22 (D6) | 60.28 | 78.17 | 77.40 | 80.09 | 79.67 | 80.00 |
| ISLES22 (D7) | 77.94 | 79.44 | 78.14 | 78.96 | 78.85 | 79.70 |
| Hanseg (D8) | 59.00 | 61.85 | 57.47 | 61.49 | 62.52 | 62.11 |
| HNTS-MRG24 (D9) | 66.73 | 65.90 | 67.65 | 63.34 | 68.00 | 68.62 |
| BRATS24 Africa (D10) | 93.07 | 92.51 | 91.97 | 92.16 | 92.36 | 92.19 |
| T2 Aneurysms (D11) | 46.76 | 41.97 | 40.16 | 44.96 | 45.48 | 47.26 |
| Avg. DSC | 69.40 | 70.40 | 69.41 | 70.94 | 71.83 | 72.37 |
| Avg. Rank | 4.64 | 4.55 | 6.27 | 4.36 | 3.18 | 2.00 |
| Dataset | Normalized Surface Distance (NSD) | | | | | |
| MS FLAIR (D1) | 78.77 | 80.16 | 79.70 | 79.57 | 79.16 | 80.03 |
| Brain Mets (D2) | 80.72 | 76.72 | 72.77 | 79.20 | 81.51 | 82.53 |
| Hippocampus (D3) | 99.46 | 99.42 | 99.43 | 99.46 | 99.39 | 99.46 |
| Atlas22 (D4) | 70.52 | 73.77 | 70.15 | 73.67 | 74.22 | 75.35 |
| CrossModa (D5) | 99.85 | 99.76 | 99.72 | 99.78 | 99.74 | 99.81 |
| Cosmos22 (D6) | 72.60 | 96.47 | 94.48 | 96.89 | 96.95 | 97.45 |
| ISLES22 (D7) | 88.55 | 90.45 | 89.39 | 90.28 | 89.59 | 90.59 |
| Hanseg (D8) | 82.20 | 85.94 | 80.44 | 85.29 | 85.94 | 85.80 |
| HNTS-MRG24 (D9) | 71.83 | 71.26 | 73.47 | 67.88 | 73.22 | 74.07 |
| BRATS24 Africa (D10) | 95.66 | 95.36 | 94.95 | 94.94 | 95.33 | 95.06 |
| T2 Aneurysms (D11) | 62.24 | 55.56 | 51.79 | 58.97 | 59.38 | 61.18 |
| Avg. NSD | 82.04 | 84.08 | 82.39 | 84.17 | 84.95 | 85.58 |
| Avg. NSD Rank | 4.27 | 4.27 | 5.82 | 4.64 | 4.00 | 2.18 |

chitecture pre-training combination may be suboptimal for the new CNN backbone.

Impact of dynamic configuration Comparing the *No (Dyn.)* and *No (Fixed)* configurations, both trained from scratch, reveals that selecting the appropriate configuration for each dataset can significantly influence performance. For instance, on datasets D2 and D11, the dynamic configuration outperforms the fixed by +7 and +5 DSC points, respectively, while for D6, the fixed configuration yields results +18 DSC points higher. In the majority of datasets where the fixed configuration underperforms relative to the dynamic nnU-Net, pre-training helps to recover performance. However, in some cases, such as with D5, the dynamic default nnU-Net still proves superior.

5.2. Ablation experiments

Low-Data Regime While previous experiments focused on comparing SSL pre-training against a from-scratch baseline with full-scale datasets available, many applications in the medical domain have access to only a very small amount of labeled images. To measure the benefits of pre-training in such a low-data regime, we artificially reduced the total

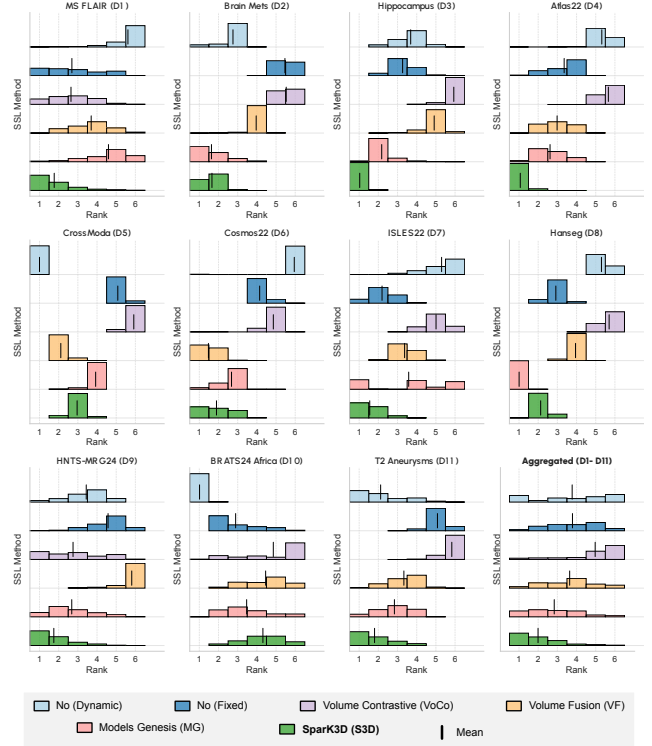


Figure 2. **S3D ranks best across all methods.** In addition to absolute mean performance, we report the ranking stability of the methods through bootstrapping for all test datasets as well as the aggregated rank across all datasets.

amount of data available for training to 10, 20, 30, or 40 labeled images.

Results are presented in Tab. 6. Our pre-trained S3D model leads to better downstream performance compared to training from scratch in this setting. With just 40 trained images, the fine-tuned model nearly matches the performance of the from-scratch model trained on the full dataset. Future research could explore whether optimizing the training duration or learning rate schedule could prevent the pre-trained network from overfitting during fine-tuning on such a limited number of training images.

Generalization Performance To assess the generalization capability of the proposed pre-training method, we tested two scenarios. First, we evaluated fine-tuning our method on an unseen modality using the TOF Angiography Aneurysms dataset (D12). As shown in Tab. 9 without pre-training, the fixed configuration suffers a performance drop of 20 Dice points. We attribute this to the significant difference in median spacing for the downstream task ([0.50, 0.43, 0.43] mm), which has a higher resolution than the fixed target spacing of [1, 1, 1] mm used in the pre-training experiments. This lower resolution likely increases

the difficulty of segmenting small aneurysms. Despite this decrease, pre-training mitigates some of this degradation and proves highly beneficial compared to training the same configuration from scratch. Interestingly, ModelGenesis achieves the best results, potentially due to its use of intensity augmentations during pre-training, which increases robustness against brightness shifts, such as when generalizing to different MRI sequences. Second, we fine-tuned on the D2 dataset using only the T1 contrast-enhanced (T1ce) sequence and applied these models directly to D13 without any additional fine-tuning. While the dynamic configuration performed best on the in-distribution validation cases of D2, the results on D13 indicate that MAE pre-training improves generalization across different centers, with our S3D model yielding the best performance.

Pre-training Time Previous studies have demonstrated the positive impact of extended training schedules on the quality of learned representations for downstream tasks [9, 14]. To explore the relevance of this factor in the 3D medical domain, we conducted a similar experiment, evaluating training durations ranging from 62.5k to 1M steps. Our results indicate that the benefits of longer training schedules begin to degrade after 250k steps, as evident in Tab. 7.

Fine-tuning length Initializing from pre-trained weights has the potential to reduce the computational resources needed for the network to adapt to new tasks. To assess this, we tested different fine-tuning durations on our development datasets. While maintaining 12.5k iterations for both the decoder and full network warm-up phases, we experimented with varying subsequent training lengths. As shown in Tab. 10, adding just 12.5k additional iterations (37.5k total) already outperforms training from scratch. However, achieving optimal performance still requires completing the full fine-tuning schedule.

Multi-Channel Input In many medical examinations, it is common to perform multiple scans, as clinicians often require images with different characteristics for accurate decision-making. Consequently, some datasets, like D2, D8, and D10, contain multiple input modalities. While pre-training may involve all modalities, we only feed one modality at a time into the network since not all patients have scans in every modality. This raises the question of how to handle datasets with multiple registered images. To address this, we conducted a 5-fold cross-validation on the D2 development dataset. We evaluated the replication of each input modality along with random initialization of the input stem weights. Additionally, we tested freezing the stem weights during the decoder warm-up phase. As shown

in Tab. 8, the most stable and consistently effective approach was replicating the pre-trained stem and keeping it frozen during the decoder’s warm-up period.

6. Conclusion

This work is the first to demonstrate the potential of properly configured MAEs in 3D medical image segmentation. By overcoming key pitfalls in previous research, such as limited dataset sizes, outdated architectures, and insufficient evaluation, we show a consistent performance improvement over previous SSL methods. Notably, for the first time, we achieve consistent improvements over the dynamic, dataset-adaptive nnU-Net baseline, validated across a large and diverse set of development and testing datasets.

Limitations In our current manuscript, we justify our selection of baseline methods by excluding prior work that was specific to architectures (3DMAE), methods that had no public code (GL-MAE), and methods that do not outperform a nnU-Net baseline trained from scratch (see Appendix Tab. 11). While our findings are promising, several avenues remain open for future exploration. We limited our method to Head and Neck MRI images, allowing us to focus on this region with a comparatively large pretraining dataset. Expanding to encompass the entire body across multiple imaging modalities would have required substantially more data to achieve comparable performance. Notably, in our ablations, we tested increasing training time and batch size (Appendix Tab. 12) which did not lead to performance improvements, but the question remains of whether scaling the pre-training dataset size or the model parameters could enable further improvements. Furthermore, the intensity shifts employed by Model Genesis SSL task hint at intriguing possibilities for improving generalization across unseen MRI modalities, which needs to be further explored for MAEs. Lastly, a data-centric approach to curating the most relevant data for SSL represents an exciting frontier for future research. Raw clinical datasets often contain images not intended for diagnostic purposes, such as those used for scanner calibration, which can dilute the effectiveness of pre-training. While we applied basic filtering to exclude low-quality data, more sophisticated filtering techniques could significantly enhance the quality of the pre-training process.

To conclude, this work follows the spirit of prior studies like nnU-Net [18] showing that a robust development strategy, informed model configuration, and rigorous validation leads to true and sustainable performance improvements, contrasting the current hype for employing and modifying the latest network architecture. With this paper, we hope to contribute to a cultural shift in the community toward validation-driven development enabling true scientific progress.

References

- [1] Michela Antonelli, Annika Reinke, Spyridon Bakas, Keyvan Farahani, Annette Kopp-Schneider, Bennett A Landman, Geert Litjens, Bjoern Menze, Olaf Ronneberger, Ronald M Summers, et al. The medical segmentation decathlon. *Nature communications*, 13(1):4128, 2022. 3
- [2] Mahmoud Assran, Quentin Duval, Ishan Misra, Piotr Bojanowski, Pascal Vincent, Michael Rabbat, Yann LeCun, and Nicolas Ballas. Self-supervised learning from images with a joint-embedding predictive architecture. In *Proceedings of the IEEE/CVF Conference on Computer Vision and Pattern Recognition*, pages 15619–15629, 2023. 1
- [3] H. Chen, X. Zhao, J. Dou, C. Du, R. Yang, H. Sun, S. Yu, H. Zhao, C. Yuan, and N. Balu. Carotid vessel wall segmentation and atherosclerosis diagnosis challenge, 2022. 3
- [4] Liang-Chieh Chen, George Papandreou, Iasonas Kokkinos, Kevin Murphy, and Alan L. Yuille. Deeplab: Semantic image segmentation with deep convolutional nets, atrous convolution, and fully connected crfs. *IEEE Transactions on Pattern Analysis and Machine Intelligence*, 2018. 3
- [5] Zekai Chen, Devansh Agarwal, Kshitij Aggarwal, Wiem Safta, Mariann Micsinai Balan, and Kevin Brown. Masked image modeling advances 3d medical image analysis. In *Proceedings of the IEEE/CVF Winter Conference on Applications of Computer Vision*, pages 1970–1980, 2023. 2, 4
- [6] Özgün Çiçek, Ahmed Abdulkadir, Soeren S Lienkamp, Thomas Brox, and Olaf Ronneberger. 3d u-net: learning dense volumetric segmentation from sparse annotation. In *Medical Image Computing and Computer-Assisted Intervention—MICCAI 2016: 19th International Conference, Athens, Greece, October 17–21, 2016, Proceedings, Part II 19*, pages 424–432. Springer, 2016. 2, 6
- [7] Reuben Dorent, Aaron Kujawa, Marina Ivory, Spyridon Bakas, Nicola Rieke, Samuel Joutard, Ben Glocker, Jorge Cardoso, Marc Modat, Kayhan Batmanghelich, et al. Crossmoda 2021 challenge: Benchmark of cross-modality domain adaptation techniques for vestibular schwannoma and cochlea segmentation. *Medical Image Analysis*, 83:102628, 2023. 3
- [8] Alexey Dosovitskiy. An image is worth 16x16 words: Transformers for image recognition at scale. *arXiv preprint arXiv:2010.11929*, 2020. 2, 4
- [9] Christoph Feichtenhofer, Yanghao Li, Kaiming He, et al. Masked autoencoders as spatiotemporal learners. *Advances in neural information processing systems*, 35:35946–35958, 2022. 4, 5, 8
- [10] Mikhail Goncharov, Vera Soboleva, Anvar Kurmukov, Maxim Pisov, and Mikhail Belyaev. vox2vec: A framework for self-supervised contrastive learning of voxel-level representations in medical images. In *Medical Image Computing and Computer Assisted Intervention – MICCAI 2023*, 2023. 15
- [11] Endre Grøvik, Darvin Yi, Michael Iv, Elizabeth Tong, Daniel Rubin, and Greg Zaharchuk. Deep learning enables automatic detection and segmentation of brain metastases on multisequence mri. *Journal of Magnetic Resonance Imaging*, 51(1):175–182, 2020. 3
- [12] Ali Hatamizadeh, Vishwesh Nath, Yucheng Tang, Dong Yang, Holger R Roth, and Daguang Xu. Swin unetr: Swin transformers for semantic segmentation of brain tumors in mri images. In *International MICCAI brainlesion workshop*, pages 272–284. Springer, 2021. 1, 2, 15
- [13] Ali Hatamizadeh, Yucheng Tang, Vishwesh Nath, Dong Yang, Andriy Myronenko, Bennett Landman, Holger Roth, and Daguang Xu. Unetr: Transformers for 3d medical image segmentation, 2021. 15
- [14] Kaiming He, Xinlei Chen, Saining Xie, Yanghao Li, Piotr Dollár, and Ross Girshick. Masked autoencoders are scalable vision learners. In *Proceedings of the IEEE/CVF conference on computer vision and pattern recognition*, pages 16000–16009, 2022. 1, 4, 5, 8, 12, 15
- [15] Yuting He, Guanyu Yang, Rongjun Ge, Yang Chen, Jean-Louis Coatrieux, Boyu Wang, and Shuo Li. Geometric visual similarity learning in 3d medical image self-supervised pre-training. In *Proceedings of the IEEE/CVF Conference on Computer Vision and Pattern Recognition*, pages 9538–9547, 2023. 2, 4
- [16] Moritz R Hernandez Petzsche, Ezequiel de la Rosa, Uta Hanning, Roland Wiest, Waldo Valenzuela, Mauricio Reyes, Maria Meyer, Sook-Lei Liew, Florian Kofler, Ivan Ezhov, et al. Isles 2022: A multi-center magnetic resonance imaging stroke lesion segmentation dataset. *Scientific data*, 9(1):762, 2022. 3
- [17] Ziyang Huang, Haoyu Wang, Zhongying Deng, Jin Ye, Yanzhou Su, Hui Sun, Junjun He, Yun Gu, Lixu Gu, Shaoting Zhang, et al. Stu-net: Scalable and transferable medical image segmentation models empowered by large-scale supervised pre-training. *arXiv preprint arXiv:2304.06716*, 2023. 1
- [18] Fabian Isensee, Paul F Jaeger, Simon AA Kohl, Jens Petersen, and Klaus H Maier-Hein. nnu-net: a self-configuring method for deep learning-based biomedical image segmentation. *Nature methods*, 18(2):203–211, 2021. 1, 2, 3, 5, 6, 8, 12, 13, 15
- [19] Fabian Isensee, Tassilo Wald, Constantin Ulrich, Michael Baumgartner, Saikat Roy, Klaus Maier-Hein, and Paul F Jaeger. nnu-net revisited: A call for rigorous validation in 3d medical image segmentation. *arXiv preprint arXiv:2404.09556*, 2024. 2, 3, 4, 13, 15
- [20] Bennett Landman, Zhoubing Xu, Juan Eugenio Iglesias, Martin Styner, and et al. 2015 miccai multi-atlas labeling beyond the cranial vault workshop and challenge. In *Proc. MICCAI Multi-Atlas Labeling Beyond Cranial Vault—Workshop Challenge*, 2015. 13, 15
- [21] Yanghao Li, Haoqi Fan, Ronghang Hu, Christoph Feichtenhofer, and Kaiming He. Scaling language-image pre-training via masking. In *Proceedings of the IEEE/CVF Conference on Computer Vision and Pattern Recognition*, pages 23390–23400, 2023. 4
- [22] Sook-Lei Liew, Bethany P Lo, Miranda R Donnelly, Artemis Zavaliangos-Petropulu, Jessica N Jeong, Giuseppe Barisano, Alexandre Hutton, Julia P Simon, Julia M Juliano, Anisha Suri, et al. A large, curated, open-source stroke neuroimaging dataset to improve lesion segmentation algorithms. *Scientific data*, 9(1):320, 2022. 3

- [23] Asbjørn Munk, Jakob Ambsdorf, Sebastian Llambias, and Mads Nielsen. Amaes: Augmented masked autoencoder pre-training on public brain mri data for 3d-native segmentation. *arXiv preprint arXiv:2408.00640*, 2024. 2, 4
- [24] Ali M. Muslim, Syamsiah Mashohor, Gheyath Al Gawwam, Rozi Mahmud, Marsyita binti Hanafi, Osama Alnuaimi, Raad Josephine, and Abdullah Dhaifallah Almutairi. Brain mri dataset of multiple sclerosis with consensus manual lesion segmentation and patient meta information. *Data in Brief*, 42:108139, 2022. 3
- [25] Maxime Oquab, Timothée Darcet, Théo Moutakanni, Huy Vo, Marc Szafraniec, Vasil Khalidov, Pierre Fernandez, Daniel Haziza, Francisco Massa, Alaaeldin El-Nouby, et al. Dinov2: Learning robust visual features without supervision. *arXiv preprint arXiv:2304.07193*, 2023. 1
- [26] Gašper Podobnik, Primož Strojjan, Primož Peterlin, Bulat Ibragimov, and Tomaž Vrtovec. Han-seg: The head and neck organ-at-risk ct and mr segmentation dataset. *Medical physics*, 50(3):1917–1927, 2023. 3
- [27] Olaf Ronneberger, Philipp Fischer, and Thomas Brox. U-net: Convolutional networks for biomedical image segmentation. In *Medical image computing and computer-assisted intervention—MICCAI 2015: 18th international conference, Munich, Germany, October 5–9, 2015, proceedings, part III 18*, pages 234–241. Springer, 2015. 2, 15
- [28] Saikat Roy, Gregor Koehler, Constantin Ulrich, Michael Baumgartner, Jens Petersen, Fabian Isensee, Paul F. Jäger, and Klaus H. Maier-Hein. Mednext: Transformer-driven scaling of convnets for medical image segmentation. In *Medical Image Computing and Computer Assisted Intervention—MICCAI 2023*, 2023. 3, 15
- [29] Amber L Simpson, Michela Antonelli, Spyridon Bakas, Michel Bilello, Keyvan Farahani, Bram Van Ginneken, Annette Kopp-Schneider, Bennett A Landman, Geert Litjens, Bjoern Menze, et al. A large annotated medical image dataset for the development and evaluation of segmentation algorithms. *arXiv preprint arXiv:1902.09063*, 2019. 3
- [30] Fenghe Tang, Ronghao Xu, Qingsong Yao, Xueming Fu, Quan Quan, Heqin Zhu, Zaiyi Liu, and S Kevin Zhou. Hyspark: Hybrid sparse masking for large scale medical image pre-training. *arXiv preprint arXiv:2408.05815*, 2024. 1, 2, 4, 13, 15
- [31] Yucheng Tang, Dong Yang, Wenqi Li, Holger R Roth, Bennett Landman, Daguang Xu, Vishwesh Nath, and Ali Hatamizadeh. Self-supervised pre-training of swin transformers for 3d medical image analysis. In *Proceedings of the IEEE/CVF conference on computer vision and pattern recognition*, pages 20730–20740, 2022. 1, 2, 4
- [32] Keyu Tian, Yi Jiang, Qishuai Diao, Chen Lin, Liwei Wang, and Zehuan Yuan. Designing bert for convolutional networks: Sparse and hierarchical masked modeling. *arXiv preprint arXiv:2301.03580*, 2023. 2, 4
- [33] Keyu Tian, Yi Jiang, Qishuai Diao, Chen Lin, Liwei Wang, and Zehuan Yuan. Designing bert for convolutional networks: Sparse and hierarchical masked modeling, 2023. 15
- [34] Zhan Tong, Yibing Song, Jue Wang, and Limin Wang. Videomae: Masked autoencoders are data-efficient learners for self-supervised video pre-training. *Advances in neural information processing systems*, 35:10078–10093, 2022. 4
- [35] Constantin Ulrich, Fabian Isensee, Tassilo Wald, Maximilian Zenk, Michael Baumgartner, and Klaus H Maier-Hein. Multitalent: A multi-dataset approach to medical image segmentation. In *International Conference on Medical Image Computing and Computer-Assisted Intervention*, pages 648–658. Springer, 2023. 1, 3
- [36] A Vaswani. Attention is all you need. *Advances in Neural Information Processing Systems*, 2017. 2
- [37] Pascal Vincent, Hugo Larochelle, Isabelle Lajoie, Yoshua Bengio, Pierre-Antoine Manzagol, and Léon Bottou. Stacked denoising autoencoders: Learning useful representations in a deep network with a local denoising criterion. *Journal of machine learning research*, 11(12), 2010. 4
- [38] Kareem Wahid, Cem Dede, Mohamed Naser, and Clifton Fuller. Training dataset for hntsmrg 2024 challenge, 2024. 3
- [39] Guotai Wang, Jianghao Wu, Xiangde Luo, Xinglong Liu, Kang Li, and Shaoting Zhang. Mis-fm: 3d medical image segmentation using foundation models pretrained on a large-scale unannotated dataset. *arXiv preprint arXiv:2306.16925*, 2023. 2, 4, 6, 12
- [40] Jakob Wasserthal, Hanns-Christian Breit, Manfred T Meyer, Maurice Pradella, Daniel Hinck, Alexander W Sauter, Tobias Heye, Daniel T Boll, Joshy Cyriac, Shan Yang, et al. Totalsegmentator: robust segmentation of 104 anatomic structures in ct images. *Radiology: Artificial Intelligence*, 5(5), 2023. 1
- [41] Sanghyun Woo, Shoubhik Debnath, Ronghang Hu, Xinlei Chen, Zhuang Liu, In So Kweon, and Saining Xie. Convnext v2: Co-designing and scaling convnets with masked autoencoders. In *Proceedings of the IEEE/CVF Conference on Computer Vision and Pattern Recognition*, pages 16133–16142, 2023. 2, 4
- [42] Linshan Wu, Jiaxin Zhuang, and Hao Chen. Voco: A simple-yet-effective volume contrastive learning framework for 3d medical image analysis. In *Proceedings of the IEEE/CVF Conference on Computer Vision and Pattern Recognition*, pages 22873–22882, 2024. 1, 2, 4, 6, 12
- [43] Xuzhe Zhang, Yuhao Wu, Elsa Angelini, Ang Li, Jia Guo, Jerod M. Rasmussen, Thomas G. O’Connor, Pathik D. Wadhwa, Andrea Parolin Jackowski, Hai Li, Jonathan Posner, Andrew F. Laine, and Yun Wang. Mapseg: Unified unsupervised domain adaptation for heterogeneous medical image segmentation based on 3d masked autoencoding and pseudo-labeling, 2024. 2, 4
- [44] Zongwei Zhou, Vatsal Sodha, Jiakuan Pang, Michael B Gotway, and Jianming Liang. Models genesis. *Medical image analysis*, 67:101840, 2021. 1, 2, 4, 6, 12
- [45] Jia-Xin Zhuang, Luyang Luo, and Hao Chen. Advancing volumetric medical image segmentation via global-local masked autoencoder. *arXiv preprint arXiv:2306.08913*, 2023. 1, 2, 4
- [46] Xinrui Zhuang, Yuexiang Li, Yifan Hu, Kai Ma, Yujiu Yang, and Yefeng Zheng. Self-supervised feature learning for 3d medical images by playing a rubik’s cube. In *Medi-*

*cal Image Computing and Computer Assisted Intervention–
MICCAI 2019: 22nd International Conference, Shenzhen,
China, October 13–17, 2019, Proceedings, Part IV 22*, pages
420–428. Springer, 2019. 4

A. Method configuration

Across all baseline methods, we utilize a common set of hyperparameters. For all baseline methods we utilize the same pre-training dataset with the same image preprocessing. Moreover we use the same amount of pre-training steps (250k) as for our S3D-B method and the same fine-tuning scheme, as highlighted in Tab. 10. Aside from this, we employ the SGD optimizer with LR $1e-2$ with a PolyLR schedule, momentum 0.99 and weight decay $3e-5$ across all pre-training experiments, as they showed to be highly robust and reliable in the supervised medical image segmentation setting using CNNs [18]. Moreover, we denote that all these methods have their backbones replaced with a ResEnc U-Net to minimize confounding effects of different architectures.

A.1. Models Genesis

Models genesis [44] pre-text task is centered around restoring original patches from transformed versions. The transformed version is achieved by applying four different transformations in various combinations, with the following transformations: a composition of four separate pre-training schemes: (i) **Non-linear intensity transformation:** Alters the intensity distribution while preserving the anatomy, focusing on learning the appearance of organs. (ii) **Out-painting:** Removes part of the image and requires the model to extrapolate from the remaining image, forcing it to learn the global structure of the organs. (iii) **In-painting:** Masks a part of the image, and the model learns to restore the missing parts, focusing on local continuity and context. After having transformed the original image through these augmentations, the model is trained to recover the original image through a convolutional encoder-decoder architecture. This approach consolidates different tasks (appearance, texture, and context learning) into one unified image restoration task, making the model more robust and generalizable.

Model specific Hyperparameters: The entire set of hyperparameters of Models Genesis are contained within the data-augmentation. This allows us to transfer this transformation pipeline, as provided in the official [repository](#) without any changes to the hyperparameters.

A.2. VolumeFusion

Volume Fusion [39] is a pseudo-segmentation task using two sub-volumes from different 3D scans, which are fused together based on random voxel-level fusion coefficients. The fused image is treated as input, and the model predicts the fusion category of each voxel, mimicking a segmentation task. Pretraining is optimized using a combination of Dice loss and cross-entropy loss.

Method specific parameters: Volume Fusion has unique parameters defining the size ranges of the rectangles used for fusing together images. In our experiments we utilize a rectangle size range between $[8, 100]$ sampled uniformly for each axis. This represent the 62.5% of our input patch size, and identical percentage as in the original paper. Moreover the amount of rectangles sampled is an important parameter. Like in the original paper we sample $M \sim \mathcal{U}(10, 40)$ different rectangles, iteratively. Lastly, the number of categories was chosen to be 5, as in the original paper (this represent $K = 4$).

A.3. VoCo

The 'Volume Contrastive Learning Framework' (VoCo) [42] is designed to enhance self-supervised learning for 3D medical image analysis by leveraging the consistent contextual positions of anatomical structures. The method involves generating base crops from different regions of 3D images and using these as class assignments. The framework then contrasts random sub-volume crops against these base crops, predicting their contextual positions using a contrastive learning approach. The authors utilize a SwinUNETR model architecture, employing the AdamW optimizer with a cosine learning rate schedule for 100,000 pre-training steps. The specific hyperparameters include cropping non-overlapping volumes with a size of $64 \times 64 \times 64$, and generating 4×4 base crops during the position prediction task. This represents an input patch size of $384 \times 384 \times 96$ which is rescaled and resized to fit exactly $4 \times 4 \times 64 \times 64 \times 64$ crops.

Since our chosen patch size $160 \times 160 \times 160$ is incompatible with the 64 cube length, we adjusted our patch size for VoCo to $192 \times 192 \times 64$. This accommodates a 3×3 grid of $64 \times 64 \times 64$. Unfortunately the 4×4 grid led to exceeding the memory limit hence a reduction was necessary. Moreover we increased the target crop size from 4 originally to 5 and increased the batch size from 6 (default in our other experiments) to 12, to fully utilize the 40GB VRAM of an A100 node.

B. Longer Training schedule

MAEs are known to benefit from increasing the length of the training schedule, as shown in He et al. [14]. We evaluate if this effect transfers to 3D medical pre-training by increasing the training batch size by $\times 8$ to 48, the learning rate to $3e - 2$, and the iteration steps by $\times 5$ to a total of $1.25M$ steps. We refer to this model as **S3D-Long** to denote the longer training schedule with more data seen. We denote that the architecture remains identical to the previous architecture, to isolate the effect of the length of the steps as well as the amount of samples seen. Results are presented in Tab. 12. It can be observed that this $\times 32$ actually leads to a decrease in overall model performance on our test datasets,

Table 5. **Public available checkpoint trained on the ABCD dataset:** To provide a public available checkpoint, we retrained our proposed model on the ABCD dataset, indicated by a *. It performs slightly worse than the network pre-trained on the private dataset.

| SSL Method | No (Dyn.) | No (Fix.) | S3D* | S3D |
|----------------------|--|--------------|--------------|--------------|
| Dataset | Dice Similarity Coefficient (DSC) | | | |
| MS FLAIR (D1) | 57.81 | <u>59.82</u> | 59.75 | 60.35 |
| Brain Mets (D2) | 63.66 | 56.53 | <u>64.20</u> | 65.24 |
| Hippocampus (D3) | 89.18 | 89.24 | <u>89.45</u> | 89.60 |
| Atlas22 (D4) | 63.28 | 65.52 | <u>66.61</u> | 66.95 |
| CrossModa (D5) | 85.64 | 83.44 | 83.61 | <u>84.08</u> |
| Cosmos22 (D6) | 60.28 | 78.17 | 80.01 | <u>80.00</u> |
| ISLES22 (D7) | 77.94 | <u>79.44</u> | 78.94 | 79.70 |
| Hanseg (D8) | 59.00 | <u>61.85</u> | 61.27 | 62.11 |
| HNTS-MRG24 (D9) | 66.73 | 65.90 | <u>67.03</u> | 68.62 |
| BRATS24 Africa (D10) | 93.07 | <u>92.51</u> | 92.49 | 92.19 |
| Avg. DSC | 71.66 | 73.24 | <u>74.34</u> | 74.88 |
| Avg. Rank | 3.2 | 2.9 | <u>2.4</u> | 1.5 |

showing a 0.6% lower average DSC as well as a 0.6% lower Average NSD.

The observed performance degradation of the S3D-Long model, despite the longer training schedule and increased data exposure, suggests several possible factors at play. While MAEs have shown benefits from extended training schedules in general computer vision tasks, the same assumptions may not directly transfer to 3D medical image pre-training due to the unique nature of this domain. The findings highlight the importance of tailoring training strategies to the domain.

C. Additional results

Aside from the quantitative data on the development and test dataset, we provide the quantitative data of the ablation experiments here. The following additional results are provided: 1. Results when fine-tuning in a low-data regime are presented in Tab. 6. 2. Experiment on how to best transfer weights when transferring to a dataset with more than 1 input channel is provided in Tab. 8. 3. Results on how the pre-training effects generalization is provided in Tab. 9. 4. Experiment results of investigating if one can reduce the fine-tuning steps are presented in Tab. 10

C.1. Public weights trained on the ABCD dataset

Due to patient privacy concerns and data ownership regulations, we are unable to share the original pre-trained weights. As an alternative, we retrained our best-performing model on the National Institute of Health’s Adolescent Brain Cognitive Development (ABCD) dataset. This dataset comprises about 41k MRI scans with a 50-to-50 ratio of T1-weighted to T2-weighted scans. The results,

Table 6. **Forty images with SSL are almost as good as all data from-scratch!** S3D model almost reaches the performance of the model trained from-scratch with only 40 training cases. * D1 has only 38 training cases for the train split.

| SSL Method | N Train | D1 | D2 | D3 | D4 | D5 | Avg. D1-D5 |
|------------|---------|--------|-------|-------|-------|-------|------------|
| Scratch | 10 | 40.78 | 43.52 | 84.94 | 44.11 | 76.66 | 58.00 |
| | 20 | 44.46 | 59.46 | 86.75 | 46.33 | 78.67 | 63.13 |
| | 30 | 45.42 | 64.20 | 87.14 | 48.22 | 78.47 | 64.69 |
| | 40 | 49.37* | 60.13 | 87.59 | 50.43 | 78.37 | 65.18 |
| | full | 49.37 | 69.13 | 88.78 | 60.74 | 81.33 | 69.87 |
| S3D (ours) | 10 | 43.48 | 48.44 | 84.12 | 41.51 | 77.70 | 59.05 |
| | 20 | 46.58 | 65.30 | 86.61 | 45.50 | 79.52 | 64.70 |
| | 30 | 48.12 | 68.41 | 86.77 | 51.62 | 78.88 | 66.76 |
| | 40 | 51.49* | 72.91 | 87.46 | 53.05 | 80.82 | 69.15 |
| | full | 51.49 | 74.01 | 88.83 | 62.39 | 81.54 | 71.65 |

Table 7. **Pre-training length ablation:** Longer pre-training does not lead to improved performance. Interestingly, when exceeding 250k steps.

| PT Iterations | D1 | D2 | D3 | D4 | D5 | Avg. D1-D5 | Train Time [h] |
|---------------|-------|-------|-------|-------|-------|------------|----------------|
| 62.5k | 49.49 | 70.79 | 88.82 | 62.95 | 81.27 | 70.67 | 28 |
| 125k | 50.56 | 70.48 | 88.86 | 62.51 | 81.69 | 70.82 | 56 |
| 250k | 51.02 | 74.07 | 88.91 | 62.81 | 81.50 | 71.66 | 112 |
| 500k | 50.93 | 72.71 | 88.88 | 62.17 | 81.86 | 71.31 | 224 |
| 1M | 50.45 | 71.55 | 88.92 | 62.78 | 81.82 | 71.10 | 448 |

Table 8. Replicating the pre-trained stem weights and freezing them during the decoder warm-up phase yields the most stable and equally best results.

| Initialization | Decoder Warm-Up | Fold 0 | Fold 1 | Fold 2 | Fold 3 | Fold 4 | Average | STD |
|----------------|-----------------|--------|--------|--------|--------|--------|--------------|------|
| Replication | Frozen | 72.84 | 64.42 | 66.11 | 62.86 | 62.85 | <u>65.82</u> | 4.15 |
| Replication | Unfrozen | 72.68 | 63.07 | 65.60 | 66.02 | 61.08 | 65.69 | 4.39 |
| Random | Frozen | 74.38 | 60.89 | 65.10 | 67.55 | 61.31 | 65.85 | 5.51 |
| Random | Unfrozen | 72.20 | 63.16 | 62.25 | 66.71 | 61.47 | 65.16 | 4.42 |

shown in Tab. 5, indicate that the original model slightly outperforms the version pre-trained on the ABCD dataset. This discrepancy is likely attributable to the greater diversity and variation in the images within our private dataset, which enables a more robust feature representation.

C.2. Comparison to previous work on CT data

Although this study focuses on brain MRI images, we also evaluate our method on a CT downstream task. Table 11 presents the results of our approach on the BTCV multi-organ segmentation task [20]. For comparison, we incorporate a diverse set of results reported in [30], which were trained using an unspecified 80/20 data split. Additionally, we fine-tune the publicly available HySpark checkpoint [30] using the same five-fold cross-validation split as for our method. Remarkably, M3D outperforms all other methods, despite being pretrained exclusively on brain MRI data. Notably, none of the related approaches surpass our backbone trained on scratch. This highlights the critical role of leveraging state-of-the-art networks and advanced training frameworks, such as nnU-Net. [18, 19].



44 Centers



8,400 Patients



43,945 Volumes

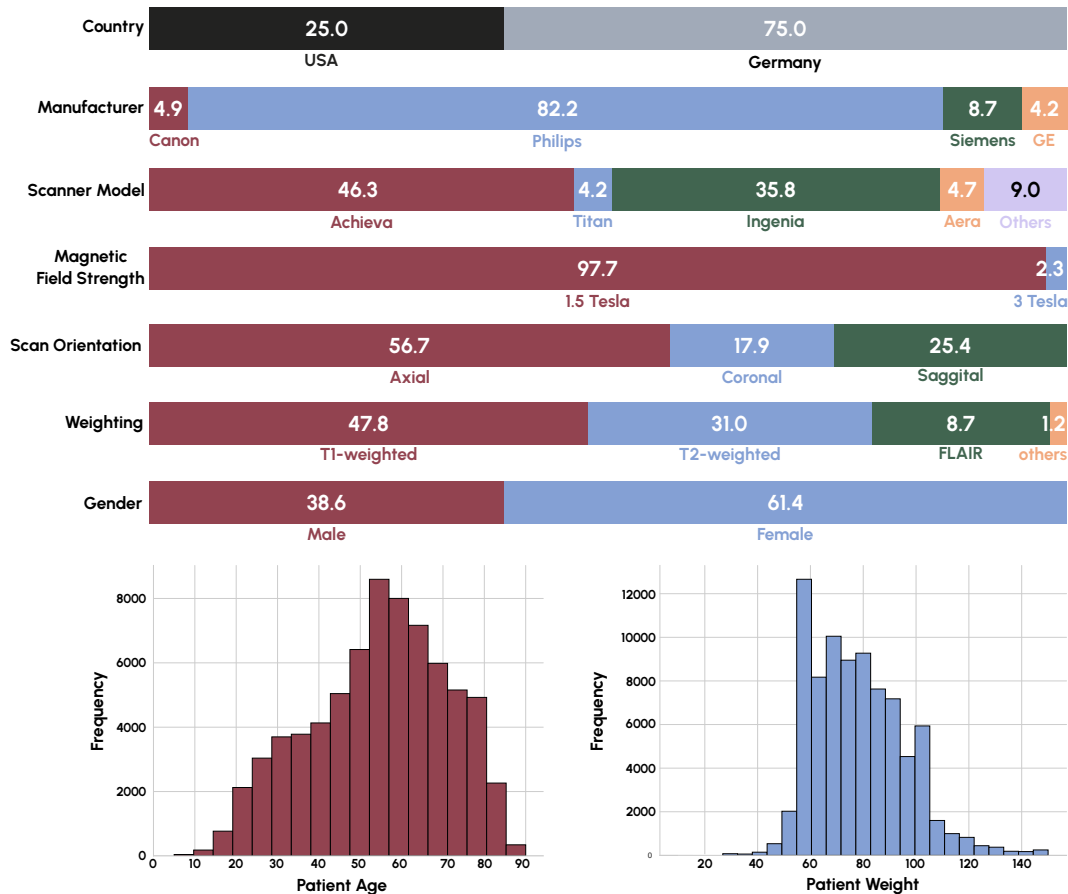


Figure 3. Distribution of our pre-training dataset. The dataset stems from 44 centers and includes 8400 Patients with a 60 to 40 female-to-male ratio. Most patients were imaged with a 1.5 Tesla Philips Achieva or Ingenia scanner. The most prevalent modalities are T1 and T2-weighted images with some additional FLAIR images present. While other modalities were in the dataset, these were not used as prevalence was deemed too low.

Table 9. **Pre-training can improve generalization:** We investigate generalization to a new modality time-of-flight (ToF) MRI (top), and the generalization of a resulting method when translating it to a different clinic (bottom).

| Experiment | Setting | No Dyn. | No Fixed | VoCo | VF | MG | S3D-B | S3D-L |
|-----------------|---------------------------|---------|----------|-------|-------|-------|-------|-------|
| Modality shift | TOF Angio. Aneurysms(D12) | 42.61 | 22.76 | 22.32 | 31.21 | 34.60 | 28.72 | 26.90 |
| In Distribution | Brain Mets (D2) | 72.81 | 67.93 | 64.34 | 71.69 | 69.05 | 71.56 | 72.53 |
| Patient shift | Brain Mets (D13) | 64.08 | 61.61 | 56.78 | 63.95 | 64.22 | 64.54 | 64.95 |

Table 10. **Fine-tuning length:** When initializing from our pre-trained checkpoint, it is possible to achieve a large fraction of the final performance after less than 15% of the normal training time. Despite this a full training schedule reaches better performance.

| FT Iterations | D1 | D2 | D3 | D4 | D5 | Avg. D1-D5 |
|---------------|-------|-------|-------|-------|-------|------------|
| 25k | 50.85 | 73.99 | 88.51 | 55.49 | 46.00 | 62.97 |
| 37.5k | 51.69 | 74.03 | 88.85 | 60.22 | 81.68 | 71.29 |
| 50k | 51.13 | 73.53 | 88.93 | 60.14 | 81.92 | 71.13 |
| 75k | 51.41 | 72.80 | 89.08 | 63.14 | 81.83 | 71.65 |
| 150k | 50.95 | 71.28 | 88.96 | 62.51 | 81.92 | 71.13 |
| 275k | 53.10 | 71.24 | 89.14 | 63.55 | 82.53 | 71.91 |

Table 11. **S3D outperforms all related work on the BTCV dataset [20].** Despite being pretrained exclusively on brain MRI data, our network outperforms all related methods. Values above the line are sourced from Tang et al. [30], which used an unknown 80/20 split. To fine-tuned their published pre-trained weights using a 5-fold cross-validation. Below the line, all models, including ours, were trained on the same 5-fold cross-validation. Notably, even though all related work leveraged CT data for pretraining, none surpassed the performance of our backbone model trained from scratch, emphasizing the importance of Pitfall 2.

| Pre-training Method | Network | Spl | Kid | Gall | Eso | Liv | Sto | Aor | IVC | Veins | Pan | AG | Avg |
|---------------------|----------------------|--------------|--------------|--------------|--------------|--------------|--------------|--------------|--------------|--------------|--------------|--------------|--------------|
| vox2vec [10] | 3D UNet(FPN) [27] | 91.40 | 90.70 | 59.50 | 72.70 | 96.30 | 83.20 | 91.30 | 83.90 | 69.20 | 73.90 | 65.20 | 79.50 |
| SUP [12] | Swin UNETR [12] | 84.20 | 86.70 | 58.40 | 70.40 | 94.40 | 76.00 | 87.70 | 82.10 | 67.00 | 69.80 | 61.00 | 75.80 |
| MAE [14] | UNETR [13] | 90.71 | 87.63 | 62.50 | 72.60 | <u>96.09</u> | 94.73 | 86.11 | 90.36 | 71.00 | 75.47 | 63.77 | 79.07 |
| SimMIM [33] | Swin UNETR [12] | 88.33 | 86.82 | 62.43 | 74.36 | 92.35 | 90.70 | 83.03 | <u>87.43</u> | 68.04 | 68.43 | 58.65 | 76.44 |
| SparK [33] | MedNeXt [28] | 90.92 | 87.66 | 62.43 | 74.36 | 95.03 | 84.85 | 86.04 | 80.63 | 68.83 | 76.57 | 61.43 | 79.21 |
| HySparK [30] | MedNeXt+ViT [30] | 90.67 | 88.32 | 68.18 | 74.20 | 95.03 | 87.46 | 90.17 | 84.50 | 70.04 | 78.36 | 66.75 | 80.67 |
| No | MedNeXt+ViT [30] | 90.35 | 87.46 | 63.18 | 74.49 | 95.09 | 86.00 | 89.29 | 83.22 | 71.85 | 79.48 | 62.59 | 80.27 |
| HySparK [30] | MedNeXt+ViT [30] | 90.94 | 86.99 | 63.43 | 74.39 | 95.12 | 87.15 | 88.92 | 83.48 | 72.77 | 79.66 | 64.84 | 80.67 |
| No (Dyn.) | nnU-Net [18] | 90.44 | 88.52 | <u>68.86</u> | 78.14 | 95.53 | 88.06 | 91.59 | 86.47 | 76.27 | 81.78 | 71.06 | 83.34 |
| No (Fix.) | ResEncL (fixed) [19] | 91.97 | 89.58 | 68.76 | 79.18 | 95.96 | 91.97 | <u>92.80</u> | 87.16 | 77.29 | <u>84.01</u> | <u>72.21</u> | <u>84.63</u> |
| S3D | ResEncL (fixed) [19] | 92.00 | <u>90.40</u> | 70.77 | <u>78.71</u> | 96.01 | <u>92.51</u> | 92.83 | 87.04 | <u>77.28</u> | 84.79 | 72.58 | 84.99 |

Table 12. **Longer training schedule degrades performance.** When training with a larger batch size, higher learning rate, and more train steps we observe a degradation in performance for DSC and NSD. Ranks are calculated only between the four methods presented in the table.

| Dataset | Dice Similarity Coefficient | | | |
|----------------------|-----------------------------|--------------|--------------|--------------|
| | No Dyn. | No Fixed | S3D | S3D-Long |
| MS FLAIR (D1) | 57.81 | 59.82 | 60.35 | <u>59.85</u> |
| Brain Mets (D2) | 63.66 | 56.53 | 65.24 | <u>64.81</u> |
| Hippocampus (D3) | 89.18 | 89.24 | 89.60 | <u>89.34</u> |
| Atlas22 (D4) | 63.28 | <u>65.52</u> | 66.95 | 64.58 |
| CrossModa (D5) | 85.64 | 83.44 | <u>84.08</u> | 84.02 |
| Cosmos22 (D6) | 60.28 | 78.17 | <u>80.00</u> | 80.01 |
| ISLES22 (D7) | 77.94 | 79.44 | <u>79.70</u> | 79.89 |
| Hanseg (D8) | 59.00 | 61.85 | 62.11 | <u>61.93</u> |
| HNTS-MRG24 (D9) | 66.73 | 65.90 | 68.62 | <u>67.94</u> |
| BRATS24 Africa (D10) | 93.07 | 92.51 | 92.19 | 92.90 |
| T2 Aneurysms (D11) | <u>46.76</u> | 41.97 | 47.26 | 44.15 |
| Avg. DSC | 69.40 | 70.40 | 72.37 | <u>71.77</u> |
| Avg. Rank | 3.09 | 3.27 | 1.55 | <u>2.09</u> |
| Dataset | Normalized Surface Distance | | | |
| | No Dyn. | No Fixed | S3D | S3D-Long |
| MS FLAIR (D1) | 78.77 | <u>80.16</u> | 80.03 | 80.40 |
| Brain Mets (D2) | 80.72 | 76.72 | 82.53 | <u>82.32</u> |
| Hippocampus (D3) | 99.46 | 99.42 | <u>99.46</u> | 99.44 |
| Atlas22 (D4) | 70.52 | <u>73.77</u> | 75.35 | 73.45 |
| CrossModa (D5) | 99.85 | 99.76 | <u>99.81</u> | 99.80 |
| Cosmos22 (D6) | 72.60 | 96.47 | 97.45 | <u>96.75</u> |
| ISLES22 (D7) | 88.55 | 90.45 | <u>90.59</u> | 90.72 |
| Hanseg (D8) | 82.20 | 85.94 | 85.80 | 86.20 |
| HNTS-MRG24 (D9) | 71.83 | 71.26 | 74.07 | <u>73.17</u> |
| BRATS24 Africa (D10) | <u>95.66</u> | 95.36 | 95.06 | 95.72 |
| T2 Aneurysms (D11) | 62.24 | 55.56 | <u>61.18</u> | 57.07 |
| Avg. NSD | 82.04 | 84.08 | 85.58 | 85.00 |
| Avg. NSD Rank | <u>2.82</u> | 3.18 | 2.00 | 2.00 |